

RESEARCH ARTICLE

10.1029/2019GC008250

Key Points:

- We compare xenon and methane hydrates in terms of equilibrium thermodynamics and nonequilibrium kinetics of hydrate growth
- Xenon hydrate has a wider nonstoichiometry region than methane hydrate, which leads to a thicker hydrate layer at the gas-liquid interface
- Hydrate nonstoichiometry coupled with hydrate formation dynamics results in a compositional gradient across the hydrate layer

Correspondence to:

X. Fu,
rubyxfu@berkeley.edu

Citation:

Fu, X., Waite, W. F., Cueto-Felgueroso, L., & Juanes, R. (2019). Xenon hydrate as an analog of methane hydrate in geologic systems out of thermodynamic equilibrium. *Geochemistry, Geophysics, Geosystems*, 20, 2462–2472. <https://doi.org/10.1029/2019GC008250>

Received 31 JAN 2019

Accepted 23 APR 2019

Accepted article online 6 MAY 2019

Published online 29 MAY 2019

Xenon Hydrate as an Analog of Methane Hydrate in Geologic Systems Out of Thermodynamic Equilibrium

Xiaojing Fu¹ , William F. Waite² , Luis Cueto-Felgueroso^{3,4} , and Ruben Juanes⁴ 

¹Department of Earth and Planetary Science, University of California, Berkeley, Berkeley, CA, USA, ²U. S. Geological Survey, Woods Hole, MA, USA, ³Department of Civil Engineering, Technical University of Madrid, Madrid, Spain, ⁴Department of Civil and Environmental Engineering, Massachusetts Institute of Technology, Cambridge, MA, USA

Abstract Methane hydrate occurs naturally under pressure and temperature conditions that are not straightforward to replicate experimentally. Xenon has emerged as an attractive laboratory alternative to methane for studying hydrate formation and dissociation in multiphase systems, given that it forms hydrates under milder conditions. However, building reliable analogies between the two hydrates requires systematic comparisons, which are currently lacking. We address this gap by developing a theoretical and computational model of gas hydrates under equilibrium and nonequilibrium conditions. We first compare equilibrium phase behaviors of the Xe-H₂O and CH₄-H₂O systems by calculating their isobaric phase diagram, and then study the nonequilibrium kinetics of interfacial hydrate growth using a phase field model. Our results show that Xe-H₂O is a good experimental analog to CH₄-H₂O, but there are key differences to consider. In particular, the aqueous solubility of xenon is altered by the presence of hydrate, similar to what is observed for methane; but xenon is consistently less soluble than methane. Xenon hydrate has a wider nonstoichiometry region, which could lead to a thicker hydrate layer at the gas-liquid interface when grown under similar kinetic forcing conditions. For both systems, our numerical calculations reveal that hydrate nonstoichiometry coupled with hydrate formation dynamics leads to a compositional gradient across the hydrate layer, where the stoichiometric ratio increases from the gas-facing side to the liquid-facing side. Our analysis suggests that accurate composition measurements could be used to infer the kinetic history of hydrate formation in natural settings where gas is abundant.

1. Introduction

Clathrate hydrates are ice-like solids crystallized from a solution of water and a hydrate former. Methane (CH₄) is the most commonly observed hydrate former in nature, and hence, methane hydrate is often referred to in geoscience contexts simply as gas hydrates. Despite their widespread occurrence and the long history of hydrate research, many questions remain regarding the precise mechanisms and processes that control the formation and growth of hydrates in multiphase systems. Addressing these fundamental knowledge gaps, in turn, is critical for understanding hydrate fabric formation in various geologic settings such as seafloor sediments and permafrost environments, devising strategies for energy extraction from geologic methane hydrate geologic reservoirs, and evaluating the fate of hydrate-crusting methane bubbles in the water column and their impact on ocean biogeochemistry.

Other compounds such as tetrahydrofuran (THF), carbon dioxide (CO₂), and xenon (Xe) can also form hydrates in the presence of water, and laboratory experiments often resort to these hydrate formers as alternatives to methane in order to recreate and understand hydrate phenomena in nature. Among these three most common analogs to methane hydrate, xenon hydrate has become increasingly popular as an experimental analog in recent years (Chaouachi et al., 2015, 2017; Chen & Espinoza, 2018; Chen et al., 2017; Jin et al., 2008; Waite et al., 2017; Yang et al., 2016). There are four main reasons for this: (1) Xenon forms structure I hydrate up to 1.8 GPa (Sanloup et al., 2002), which is the hydrate structure commonly observed in nature; (2) xenon remains a gas phase under relevant experimental conditions (in contrast to THF, which is a liquid that is fully miscible with water and therefore poorly suited for studies of interfacial growth and multiphase dissociation of hydrate); (3) xenon is nonflammable and can be used to form hydrates under ambient temperature and moderate pressure (e.g., 24 °C and 7 MPa), experimental conditions which are

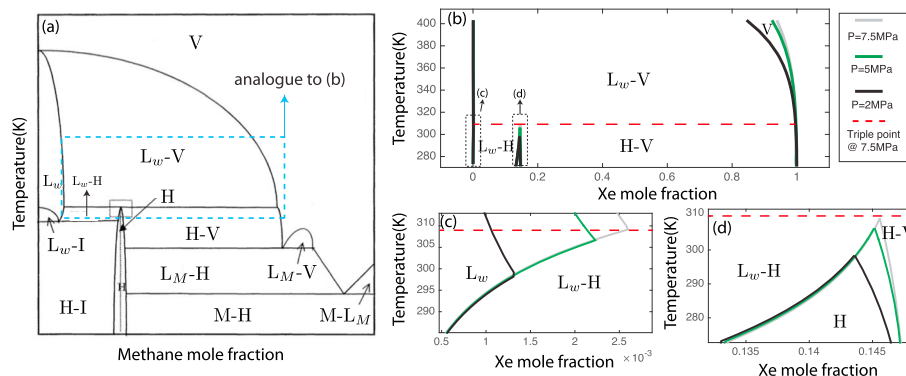


Figure 1. T- χ phase diagram for (a) CH₄-H₂O at $p = 5$ MPa, adapted from Huo et al. (2003); (b) Xe-H₂O at $p = 2$ MPa, 5 MPa and 7.5 MPa, calculated by CSMGem. Close-up view of (b) focusing on (c) the aqueous-hydrate phase boundaries and (d) hydrate-only region (H) for different pressures. (V = vapor, L_w = liquid water, H = hydrate, M = solid methane, L_M = liquid methane, I = ice.)

easier to create and control in the laboratory relative to what is required for methane hydrate; and (4) due to its high molecular mass (131.3 g/mol), xenon gas can enhance the density contrast between gas hydrate and the aqueous solution, thus significantly improving image quality when using X-ray computed tomography (CT). Although there are compelling reasons for using xenon as an alternative to methane, the validity of this analogy remains to be examined. While there have been studies comparing THF and CO₂ hydrates with methane hydrate (Lee et al., 2007; Lei & Santamarina, 2018), a systematic study comparing xenon and methane hydrates is still missing. The goal of this paper is to address this gap with a comprehensive comparison between xenon and methane hydrates, specifically regarding their equilibrium thermodynamics and nonequilibrium kinetics.

We first study equilibrium thermodynamics using CSMGem (Ballard & Sloan, 2002, 2004a, 2004b; Jager et al., 2003) to compute the isobaric phase diagram for the Xe-H₂O and CH₄-H₂O systems. We validate relevant regions of the calculated phase diagram against existing laboratory measurements. We then investigate the nonequilibrium growth dynamics of interfacial hydrates on a gas-liquid interface, using the modeling framework recently proposed by Fu et al. (2018). Our focus here is on comparing the phase transition behaviors of the two systems. Based on our results, we argue that Xe-H₂O is a good experimental analog for CH₄-H₂O systems, both in terms of the equilibrium thermodynamic behaviors and the nonequilibrium kinetics of hydrate growth in multiphase systems. We note that xenon hydrate may differ from methane hydrate in terms of mechanical and thermal properties, and we do not address these differences in the current paper.

2. Equilibrium Phase Behaviors

We use CSMGem to calculate the temperature (T)—composition (χ) phase diagram for the Xe-H₂O system at three different pressures: 2, 5, and 7.5 MPa (Figure 1b). The same calculation for the CH₄-H₂O system has been performed by others using CSMGem (Ballard & Sloan, 2002, 2004a; Jager et al., 2003) or similar methods (Zatsepina & Buffett, 1997, 1998) (Figure 1a, at $p \approx 5$ MPa). The phase boundaries in the phase diagrams exhibit similar structures in the region above the freezing point of water (blue dashed box in Figure 1a). Specifically, along the temperature axis, this region is divided by the triple-point temperature into two sections: hydrate-free region (above the triple point) and hydrate-stable region (below the triple point). The hydrate-free region is further divided by two-phase boundaries into three zones: liquid-only (L_w), liquid-vapor coexistence (L_w-V), and vapor-only (V). The two-phase boundaries continue into the hydrate-stable region, where the L_w-V is reconfigured by two additional phase boundaries into three new zones: liquid-hydrate coexistence (L_w-H), hydrate-only (H), and hydrate-vapor coexistence (H-V). Below, we perform a detailed comparison between the Xe-H₂O and CH₄-H₂O systems for the hydrate-stable region (Figures 1c and 1d).

2.1. Solubility in the Presence of Hydrates

As we zoom into the aqueous-hydrate-phase boundaries for xenon (Figure 1c), we observe that the solubility of xenon experiences a nonmonotonic trend as temperature traverses through the triple point. This

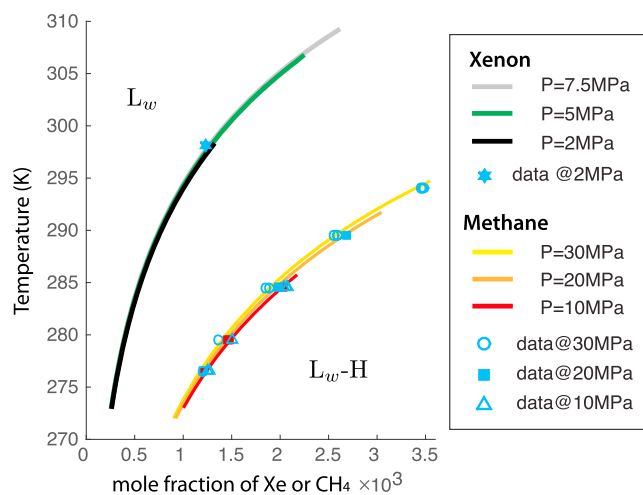


Figure 2. Aqueous solubility in the presence of hydrate calculated by CSMGem for xenon (top three curves) and methane (bottom three curves). Experimental measurements for xenon taken from Kennan and Pollack (1990) and for methane taken from Lu et al. (2008).

aqueous-hydrate-phase boundary feature also exists for $\text{CH}_4\text{-H}_2\text{O}$ and $\text{CO}_2\text{-H}_2\text{O}$ systems (Zatsepina & Buffett, 1997, 1998). This indicates that aqueous solubility is significantly altered in the presence of hydrate, where it decreases sharply with decreasing temperature once the temperature is below the triple point. The sudden decrease in solubility around the triple point allows hydrate to form directly from an aqueous solution without free gas present (Collett et al., 2009), a feature that can be exploited in the laboratory to mimic naturally-occurring hydrate in sediment (Buffett & Zatsepina, 2000; Priegnitz et al., 2015; Spangenberg & Kulenkampff, 2006; Waite & Spangenberg, 2013).

Next, we directly compare aqueous solubility in the presence of hydrate for xenon and methane systems, along with existing experimental measurements (Figure 2). For the methane system, theoretical predictions agree with the data at all pressures from Lu et al. (2008). The same is true for xenon at 2 MPa (Kennan & Pollack, 1990). From Figure 2, it is evident that xenon solubility in the presence of hydrate is, in general, smaller than that of methane, but both systems exhibit a decreasing solubility with decreasing temperature in this region.

2.2. Hydrate Nonstoichiometry

Methane hydrate is known to be a nonstoichiometric solid with variable cage occupancy (Huo et al., 2003; Sloan & Koh, 2008; Sloan et al., 2010)

($\text{CH}_4 \cdot 5.75\text{H}_2\text{O}$ for 100% cage occupancy). Based on its chemical formula, the theoretical mole fraction of methane in hydrate is computed as

$$\chi_{\text{stoich.}} = \frac{1 \text{ mol CH}_4}{1 \text{ mol CH}_4 + 5.75 \text{ mol H}_2\text{O}} \approx 0.148. \quad (1)$$

In practice, however, methane mole fractions in the hydrate phase are smaller than 0.148 and vary depending on the composition of the feeding phase (Huo et al., 2003). Such nonstoichiometric behavior is clearly evident in the T - χ phase diagram for methane (Figure 3, bottom three curves), where the hydrate-only region (labeled H) takes on a distinct triangular shape. The triangular region is formed by the L_w -H and H-V phase boundaries, which converge at the triple point.

The T - χ phase diagram for xenon hydrate ($\text{Xe}\cdot 5.75\text{H}_2\text{O}$ for 100% cage occupancy) shows similar nonstoichiometric behaviors (Figure 3, top three curves) to those of methane. We find that the difference in cage occupancy between gas-facing and liquid-facing hydrates is consistently larger for xenon than for methane. Specifically, at 2 MPa and 275 K, gas-facing xenon hydrate ($\chi_{\text{eq}} \approx 0.147$) is expected to have 10% more xenon than liquid-facing hydrate ($\chi_{\text{eq}} \approx 0.134$). We also compare experimental measurements of the Xe- H_2O triple point as reported by Ohgaki et al. (2000; Figure 3, dashed lines) and find they agree well with the theoretical prediction by CSMGem.

Our results thus far have demonstrated that hydrate nonstoichiometry is a robust feature predicted by equilibrium thermodynamics for both xenon and methane hydrates and has been partially validated by experimental measurements. The separation of the two-phase boundaries is an equilibrium prediction, but as we discuss in the next section, the departure from stoichiometric relations has significant implications on the nonequilibrium growth dynamics of interfacial hydrates in both methane and xenon systems.

3. Nonequilibrium Growth of Hydrates on Gas-Liquid Interfaces

When free gas is present in an aqueous environment, hydrate can grow on the gas-liquid interface. During such growth, however, the entire interface is out of thermodynamic equilibrium over laboratory time scales (hours to weeks) due to slow diffusion of gas and water molecules through the hydrate phase (Huo et al., 2003). Slow diffusion through interfacial hydrate significantly impacts how gas is transported through the water column or within sediments. The phenomena of hydrate-crusting gas bubbles in the water column (Warzinski et al., 2014; Wang et al., 2016; Waite et al., 2017) or crustal gas pockets in the sediment (Chen et al., 2017; Lei & Santamarina, 2018; Meyer, Flemings, & DiCarlo 2018; Meyer, Flemings, DiCarlo, et al., 2018; Sahoo, Marín-Moreno, et al., 2018; Sahoo, Madhusudhan, et al., 2018) have been widely observed

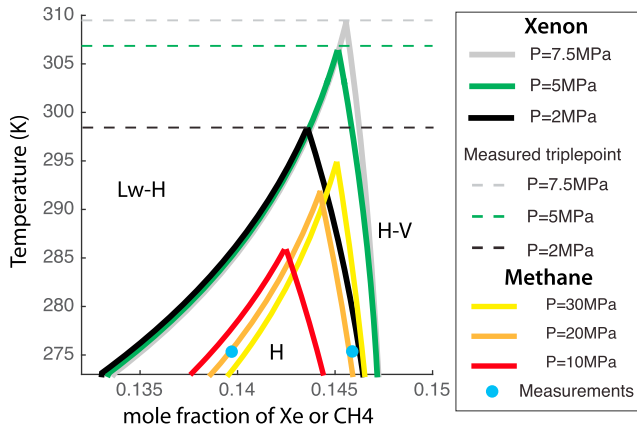


Figure 3. Phase diagram calculated with CSMGem for Xe-H₂O (top three curves) and CH₄-H₂O (bottom three curves) at different pressures. The triple-point temperatures for xenon at different pressures (dashed lines) represent experimental data from Ohgaki et al. (2000) and are in excellent agreement with CSMGem predictions. Blue circles are Raman spectroscopy measurements of methane mole fraction within a hydrate layer at $T = 275.15$ K and 30 MPa from Huo et al. (2003).

and allude to the prolonged coexistence of gas, liquid, and hydrate phases (three-phase coexistence) that is not predicted by the equilibrium-phase diagram (Fu et al., 2018). Although the three-phase configuration across the interface is out of equilibrium, the two boundaries of the growing hydrate layer can independently approach local equilibria with the phase it contacts (gas or liquid). In particular, hydrate nonstoichiometry indicates that hydrate growing into the gas phase (composition determined by H-V equilibrium) has a higher methane mole fraction than hydrate growing into the aqueous phase (composition determined by Lw-H equilibrium). Better understanding and characterization of nonstoichiometry in natural hydrates is crucial to improving our current estimates of the global methane inventory stored in hydrate form on Earth (Ruppel & Kessler, 2017; Sloan et al., 2010). It also suggests that accurate measurement of cage occupancy in naturally formed hydrates may be used to determine the formation conditions of hydrates in the past: hydrates formed out of saturated water are expected to contain less methane than those formed in the presence of free gas (see section 3.3.3). Thus, a nonequilibrium framework is necessary in order to understand interfacial hydrates. Here we use the model recently proposed in Fu et al. (2018) to study the nonequilibrium nature of interfacial hydrate growth for both methane and xenon systems.

3.1. Continuum Theory of Gas-Liquid-Hydrate System Out of Equilibrium

We have recently developed a continuum-scale phase field model to study gas-liquid-hydrate systems far from thermodynamic equilibrium (Fu et al., 2018). In this framework, we denote by ϕ_α the volumetric fractions of phase α , where $\alpha = g, l, s$ refers to the gas, liquid, and solid hydrate phase, respectively. At any given point in the continuum domain, they satisfy $\phi_g + \phi_l + \phi_s \equiv 1$. The system is also characterized by the point-wise mole fraction of CH₄ or Xe: $\chi = N_{\text{CH}_4 \text{ or Xe}} / (N_{\text{CH}_4 \text{ or Xe}} + N_{\text{H}_2\text{O}})$. We start by designing a simplified version of the Gibbs free energy functional for the three phases as a function of χ and temperature (T in Kelvin):

$$f_l(\chi, T) = \omega_{\text{mix}} \{ \chi \log(\chi) - (1 - \chi) \log(1 - a_l(T)\chi) - \chi \log(1 - b_l(1 - \chi)) \} + f_{l0}, \quad (2)$$

$$f_g(\chi, T) = \omega_{\text{mix}} \{ \chi \log(\chi) - (1 - \chi) \log(1 - a_g\chi) - \chi \log(1 - b_g(T)(1 - \chi)) \} + f_{g0}, \quad (3)$$

$$f_s(\chi, T) = \omega_{\text{mix}} \{ a_s(T)(\chi - \chi_s)^2 + b_s(T) \} + f_{s0}, \quad (4)$$

where ω_{mix} (J/cm³) is a characteristic energy density. We account for the nonlinear temperature dependence of f_α through its parameters, as suggested by Wilson (1964) for gas and liquid (equations (2) and (3)), and as suggested in the solidification literature (Cogswell & Carter, 2011; Moelans, 2011; Nestler et al., 2000) for the solid phase (equation (4)): $a_l = a_{l0}/(T/T_c)^4$, $b_g = b_{g0}/(T/T_c)^2$, $a_s = a_{s0}/(T/T_c)$, and $b_s = b_{s0}/(T/T_c)$. Here T_c is the triple-point temperature, which we use as the characteristic temperature to scale the temperature dependence of the free energy.

Under the phase field framework, the f_α 's are incorporated into the total free energy $F(\chi, \phi, T)$, which considers the energetic interactions between phases and is composed of the bulk free energy f_0 and the interfacial energy (gradient-square terms):

$$F = \int_V \left[f_0(\chi, \phi, T) + \epsilon_\chi^2(T) |\nabla \chi|^2 + \epsilon_{gl}^2(T) \nabla \phi_g \cdot \nabla \phi_l + \epsilon_{gs}^2(T) \nabla \phi_g \cdot \nabla \phi_s + \epsilon_{sl}^2(T) \nabla \phi_s \cdot \nabla \phi_l + \epsilon_g^2(T) |\nabla \phi_g|^2 + \epsilon_l^2(T) |\nabla \phi_l|^2 + \epsilon_s^2(T) |\nabla \phi_s|^2 \right] dV. \quad (5)$$

Table 1
Parameters Used in the Gibbs Free Energy Calculations for Methane and Xenon Systems

	P (MPa)	T_c [K]	a_g	b_{g0}	f_{g0}	a_{l0}	b_l	f_{l0}	a_{s0}	χ_s	b_{s0}	f_{s0}
CH ₄	30	295	1	-8.7×10^{-5}	-20	-7.57	1	-20	3.54×10^5	0.146	191.75	-40
Xe	7.5	309	0.1	-9.55×10^{-6}	-6	0.0912	0.1	-2	2.01×10^6	0.146	200.85	-63

Here, f_0 is the bulk free energy density of all the phases and the gradient-square terms in F consider the mean field interactions between each phase pair and between the two chemical components (Fu et al., 2018). The proposed free energy F is incorporated into a phase field model to study the nonequilibrium thermodynamics of the three-phase system. The evolution of the system variables (χ and ϕ_α 's) is driven by potentials Ψ , which are variational derivatives of F :

$$\Psi_\chi = \frac{\partial F}{\partial \chi} - \nabla \cdot \frac{\partial F}{\partial \nabla \chi} \quad (6)$$

$$\Psi_{\phi_\alpha} = \frac{\partial F}{\partial \phi_\alpha} - \nabla \cdot \frac{\partial F}{\partial \nabla \phi_\alpha}, \quad \alpha = g, l, s \quad (7)$$

Here we employ a Cahn-Hilliard-type equation (Cahn & Hilliard, 1958) to describe the molar conservation of the hydrate former (equation (8)), where diffusion is the sole process that transports CH₄ or Xe. We then use three Allen-Cahn-type equations to describe the changes in phase volume fractions due to phase transitions (equation (9)), which give rise to reaction-type kinetics. We close the system with the constraint that enforces conservation of phase fractions (equation (10)).

$$\frac{\partial \chi}{\partial t} - R_\chi \nabla \cdot (D(\phi) \nabla \Psi_\chi) = 0, \quad (8)$$

$$\frac{\partial \phi_\alpha}{\partial t} + R_{\phi_\alpha} \Psi_\alpha = 0, \quad \alpha = g, l, s, \quad (9)$$

$$\phi_l + \phi_g + \phi_s \equiv 1. \quad (10)$$

Here, R_χ is the effective rate of diffusion, R_{ϕ_α} is the rate of phase change for phase α , and $D(\phi) = \phi_g D_g + \phi_l D_l + \phi_s D_s$ is a dimensionless mixture diffusion coefficient (where D_g , D_l , and D_s are normalized by a characteristic gas-phase diffusion coefficient D_{gas}). We adopt $D_g = 1$, $D_l = 10^{-3}$ and $D_s = 10^{-11}$ (whose relative magnitudes are consistent with experimental measurements, Peters et al., 2008; Witherspoon & Saraf, 1965, and emulate slow diffusion in liquid and extremely slow diffusion within hydrate).

We note that the model presented here (1) assumes isothermal conditions; (2) assumes negligible compressibility so that the evolution is sufficiently slow to allow for pressure dissipation at the relevant length scale for hydrate formation (μm to mm)—a reasonable assumption given the slow kinetics of hydrate formation; and (3) neglects volume change upon mixing and reaction. While it is not straightforward to substantiate this last assumption quantitatively, we show below that the model captures key features of the gas-liquid-hydrate system under nonequilibrium conditions.

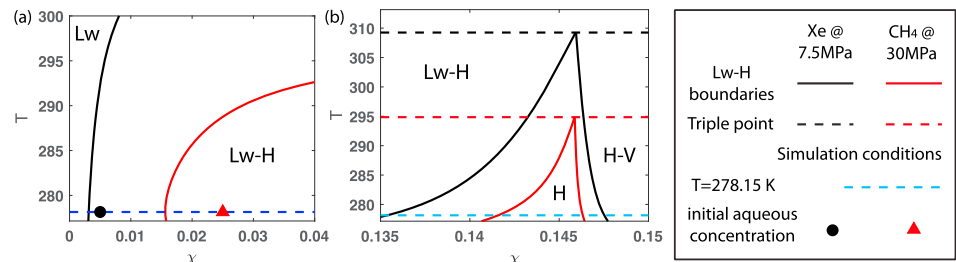


Figure 4. Equilibrium phase diagram calculated by our model for the CH₄-H₂O system at 30 MPa (red curve) and the Xe-H₂O system at 7.5 MPa (black curve). Zoomed-in view of (a) the aqueous-hydrate-phase boundary and (b) the hydrate region. For simulations performed in section 3.3, the blue dashed line marks the assumed temperature, the black dot and red triangle mark the initial aqueous mole fraction of Xe and CH₄, respectively.

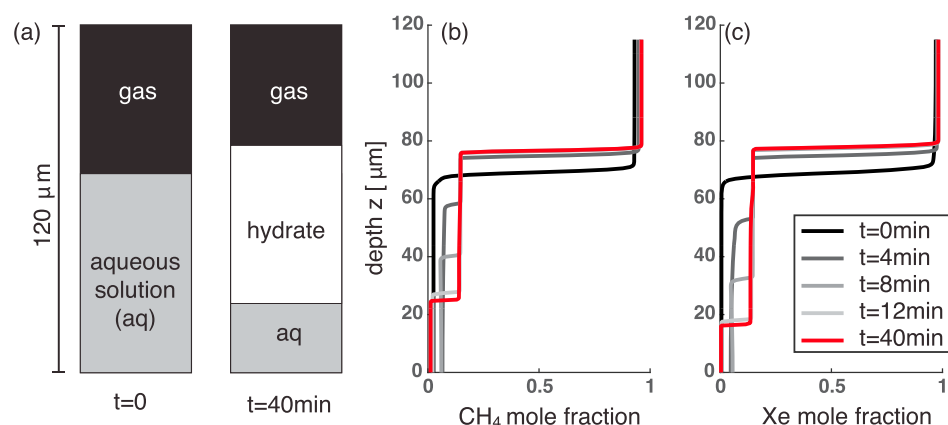


Figure 5. (a) Simulation setup at $t = 0$ min and quasi steady state configuration at $t = 40$ min. The simulation parameters are given in Figure 4 and Table 1. Snapshots of the χ profile at different times are shown for (b) CH_4 and (c) Xe.

3.2. Isobaric Phase Diagram

Based on the simplified Gibbs free energy (equations (2)–(4)) and the calibrated parameters reported in Table 1, we calculate the aqueous-hydrate-phase boundary for the CH_4 - H_2O system at 30 MPa (Figure 4a, red curve) and the Xe- H_2O system at 7.5 MPa (Figure 4a, black curve). In comparison to CSMGem calculations in Figures 1c and 2, aqueous solubility in the presence of hydrate as predicted by our model is 10 times higher. However, the model correctly predicts the general trend that solubility decreases with decreasing temperature below the triple point and predicts a smaller solubility for Xe than for CH_4 in the presence of hydrate. Figure 4b illustrates our model calculation of the hydrate region (H) for CH_4 - H_2O and Xe- H_2O systems, both of which agree well with predictions performed by CSMGem (Figures 1 and 3).

3.3. Hydrate Growth on a Gas-Liquid Interface

The growth of interfacial hydrate layer is a ubiquitous process in hydrate systems and plays a crucial role in the multiphase transport of gas in both natural (Warzinski et al., 2014; Wang et al., 2016) and engineering settings (Sum et al., 2012). In particular, understanding the growth rate and ultimate thickness of the hydrate layer is key to characterizing the time and spatial scales at which hydrate layers impact the buoyant flow of gas in seafloor sediments and the ocean water column. Existing studies have focused on using experimental methods to quantify how subcooling (Freer et al., 2001; Li et al., 2014; Tanaka et al., 2009) and

salt concentrations (Jung & Santamarina, 2012) impact hydrate layer growth rate and its thickness. Here we investigate this problem using nonequilibrium theory and numerical simulation. Specifically, we perform 1-D simulations of hydrate layer growth on a gas-liquid interface for both CH_4 and Xe at 278.15 K and investigate (1) hydrate growth kinetics, (2) the impact of hydrate nonstoichiometry on layer thickness, and (3) compositional heterogeneity within hydrate layers.

The system of four partial differential equations (PDEs) in equations (8) and (9) is discretized using finite elements and a monolithically coupled implicit time integration scheme. The simulation is performed in a 1-D domain with a 120- μm height (Figure 5a, $t = 0$). Initially, the bottom 72 μm of the domain is filled with liquid water that is slightly oversaturated with respect to solubility in the presence of hydrate (circular and triangular markers in Figure 4a). The top 48 μm of the domain is filled with gas that is slightly oversaturated in water with respect to the H-V equilibrium. We perform the simulation up to 40 min, during which time a hydrate layer grows at the interface (Figure 5a, $t = 40$ min).

3.3.1. Hydrate Growth Kinetics

Snapshots of the χ profile across the entire interface (not specific to any phase) for both simulations (Figures 5b and 5c) illustrate the development of three distinct compositional regions in the domain as the hydrate

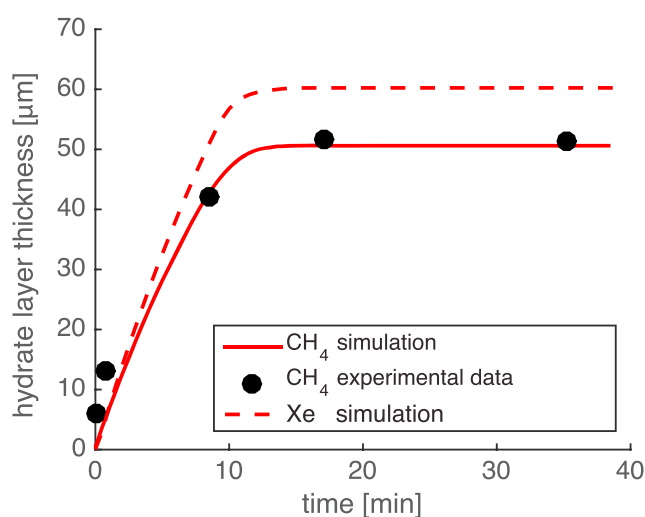


Figure 6. Hydrate layer thickness as a function of time for CH_4 (solid line) and Xe (dashed line). The black dots are data measured for CH_4 hydrate under similar experimental conditions (Taylor et al., 2007).

Table 2
Parameters Used for 1-D Simulations of CH₄ and Xe

R_χ (cm ² /s·J)	R_{ϕ_g} (1/s·J)	R_{ϕ_l} (1/s·J)	R_{ϕ_s} (1/s·J)
2.7×10^{-9}	2.38×10^{-5}	2.38×10^{-5}	2.97×10^{-5}

layer grows, reflecting the contrasting mole fractions of CH₄ or Xe in liquid ($\chi \ll 0.01$), gas ($\chi \gg 0.99$), and hydrate ($\chi \approx 0.148$). The rate of diffusion of CH₄ or Xe within hydrate is extremely slow compared to that in gas or liquid. For this reason, the growth of hydrate on a gas-liquid interface results in a mass transport barrier that dramatically reduces hydrate growth rate. Macroscopically, this is evident because as one measures the thickness of interfacial hydrate layers over time, one finds the layers grow to quasi steady state thicknesses after some initial period (Taylor et al., 2007). This behavior is well captured by our model (Figure 6). In practice, however, micropores and other discontinuities in the hydrate layer could enable mass transport across the hydrate layer and facilitate continued layer growth (Jung & Santamarina, 2012).

3.3.2. Hydrate Layer Thickness

We investigate the impact of hydrate nonstoichiometry on the quasi steady state layer thickness. We use parameters in Table 2, which are calibrated from methane experiments (Taylor et al., 2007) and apply the same parameters for both simulations of xenon and methane. This assumption means the kinetic forcing is comparable in both simulations (e.g., similar subcooling/solidification rate). We record the thickness of

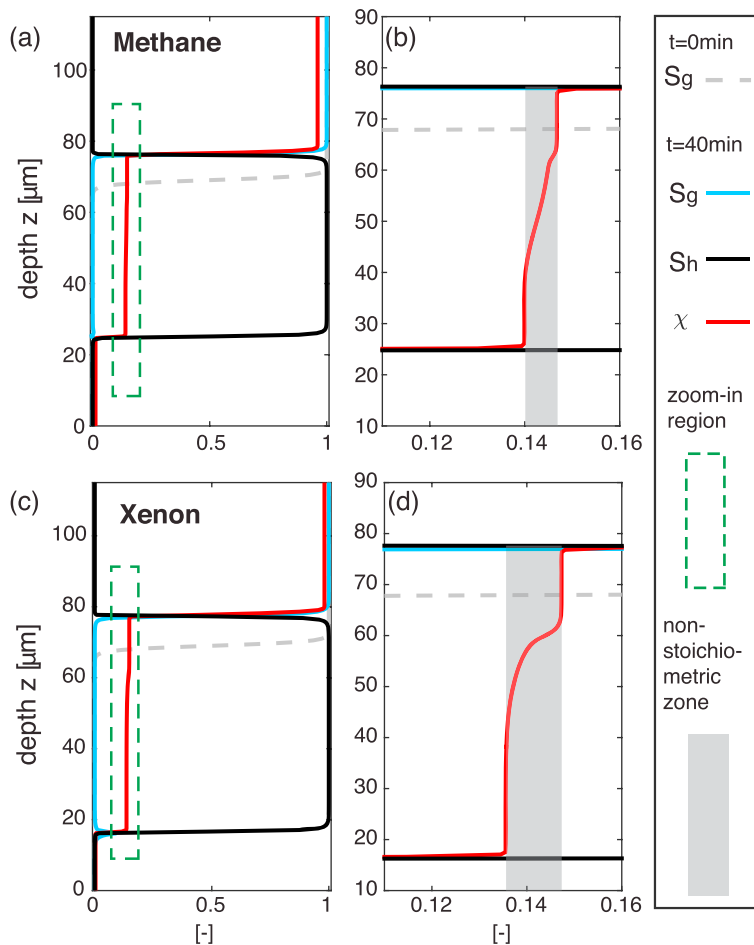


Figure 7. At $t = 40$ min, profiles for ϕ_g (blue), ϕ_s (black) and χ (red) are shown for (a, b) CH₄ and (c, d) Xe. The detailed compositional profile within the hydrate layer (dashed green boxes in a and c) are shown for CH₄ (b) and Xe (d). The shaded region in (b) and (d) highlights the gradient in χ across the hydrate layer due to hydrate nonstoichiometry. The gray dashed lines in all sub figures is the ϕ_g profile at $t = 0$, marking the initial gas-liquid interface.

the hydrate layer over time for both simulations, and compare the result with experimental measurements conducted under similar conditions for methane by Taylor et al. (2007; Figure 6).

After a brief period of nucleation, the layer growth slows down and the layer thickness plateaus after approximately 10 minutes (Figure 6). It is apparent from the simulations that, under comparable growth kinetic conditions, the xenon hydrate layer is thicker than that of methane hydrate. We conjecture this is due to a wider nonstoichiometry region for xenon hydrate, as shown in Figures 3 and 4b, which implies that a lower concentration of xenon than methane is required in the aqueous phase to maintain equilibrium with the overlying hydrate (Figure 5a). Consequently, after gas partially dissolves into the aqueous phase at the gas-liquid interface, creating a locally supersaturated region (Figures 5b and 5c, 4 and 8 min), there is relatively more xenon than methane available for hydrate to grow from the dissolved phase. This allows xenon hydrate to grow over a wider concentration range and form more hydrate than the methane system.

3.3.3. Compositional Gradient Within the Hydrate Layer

As the hydrate solidification front advances starting from the initial gas-liquid interface, the amount of CH_4/Xe that is required locally to form hydrate is recorded in the profiles of χ . Take the $\text{CH}_4\text{-H}_2\text{O}$ system at 30 MPa, 278.15 K, for example. At the gas-facing front, hydrate composition is predicted by the H-V equilibrium to be $\chi_{\text{eq}}^{\text{H-V}} \approx 0.147$. At the liquid-facing front, hydrate composition is predicted by the $\text{L}_w\text{-H}$ equilibrium to be $\chi_{\text{eq}}^{\text{H-V}} \approx 0.139$. As a result of such nonstoichiometry in hydrate composition, the amount of CH_4 required to form hydrate is different for the gas-facing and the liquid-facing hydrate front. Thus, there will be a gradient in χ across the formed hydrate layer, descending from the gas-facing side to the liquid-facing side. The work by Huo et al. (2003) has provided preliminary experimental evidence of such a gradient: they measured CH_4 mole fraction close to the gas-facing and liquid-facing end of the hydrate layer (Figure 3, blue dots) and confirmed they are indeed different. Here we show that our computational model also predicts a compositional gradient within the growing hydrate layer. Indeed, the profiles of χ at $t = 40$ min exhibit a monotonic decreasing trend from the gas-facing front (above the dashed gray line) to the liquid-facing front (below the dashed gray line) of the hydrate layer for both methane (Figure 7b) and xenon (Figure 7d), in agreement with experimental results. Because xenon has a more pronounced nonstoichiometry region than methane, the gradient also spans a wider range of χ values and spatial scales.

4. Conclusions

Xenon hydrate is an attractive laboratory alternative to methane hydrate in studying gas hydrate formation and dissociation behaviors in controlled settings, and this study provides some of the first comparative work with which to assess the validity of xenon as an analog for methane in gas hydrate research. This paper specifically targets studies of equilibrium thermodynamics and nonequilibrium kinetics, using theoretical and numerical modeling approaches. By comparing equilibrium phase behaviors of $\text{Xe-H}_2\text{O}$ and $\text{CH}_4\text{-H}_2\text{O}$ systems based on isobaric-phase diagram generated by CSMGem, we show that the aqueous solubility of xenon is altered by the presence of hydrate, similar to that of methane. Surprisingly, we find that xenon solubility in the presence of hydrate is smaller than that of methane and that xenon hydrate has a more pronounced nonstoichiometry region compared to methane hydrate.

Using a recently proposed continuum-scale phase field model, we then investigate the implications of hydrate nonstoichiometry in the nonequilibrium kinetics of interfacial hydrate growth for both methane and xenon. Our model captures the diffusion-limited hydrate growth kinetics as measured by experiments, which explains why the hydrate layer forming at the gas-liquid interface adopts a quasi steady state thickness in many laboratory studies. When growing under similar kinetic forcing conditions, our model predicts that the xenon hydrate layer becomes thicker than that of methane hydrate. We explain such differences with the observation that xenon has a more pronounced nonstoichiometry region than methane, allowing hydrate to grow over a wider range of compositions. Our numerical calculation is also validated by existing laboratory observations by Huo et al. (2003), which shows that hydrate nonstoichiometry results in a compositional gradient across the hydrate layer formed in a three-phase environment.

The observed stoichiometry dependence on hydrate formation environment has practical implications for studying laboratory and natural occurrences of gas hydrate, because researchers often assume a fixed stoichiometry in order to link the volume of hydrate to the volume of gas stored in that hydrate (Sloan et al., 2010). Circone et al. (2005) investigated the composition of methane hydrate by melting fine grains of ice in a pressurized methane atmosphere. This “hydrate from ice” method, developed by Stern et al. (1996), is

designed to maximize the surface area of gas-water contact, where the entire hydrate formation process is assumed to occur (e.g., the upper interface in Figure 7a). As anticipated from Figure 4b and 7b, the resulting hydrate, which formed in a gas-abundant environment, has a relatively high methane concentration of $\chi \approx 0.145 \pm 0.001$, given by Circone et al. (2005) as a stoichiometric ratio of $\text{CH}_4 \cdot (5.89 \pm 0.06)\text{H}_2\text{O}$. They also noted their methane concentrations were higher than those of Huo et al. (2003), which measured the concentration in hydrate grown from the aqueous side to be $\chi \approx 0.139 \pm 0.001$, or $\text{CH}_4 \cdot (6.2 \pm 0.06)\text{H}_2\text{O}$ (Huo et al., 2003; see Figure 4b).

Figure 4b provides the basis for converting hydrate volume to stored gas volume during the formation process. In particular, it is appropriate to assume $\chi \approx 0.145$ as long as the formation process takes place in a gas-excess environment (Circone et al., 2005; Stern et al., 1996). However, where hydrate is formed from dissolved phase methane in the laboratory (Priegnitz et al., 2015; Spangenberg & Kulenkampff, 2006) or in nature, assuming $\chi \approx 0.145$ would underestimate the volume of hydrate formed from dissolved-phase methane by 4% (assume 10 MPa, 4 °C). In a gas-limiting equilibrium environment, it is more appropriate to assume $\chi \approx 0.139$ (at 10 MPa), as suggested by theoretical calculations (Figure 3). This also agrees well with laboratory studies, which measure $0.138 < \chi < 0.140$, or $\text{CH}_4 \cdot (6.14\text{--}6.25)\text{H}_2\text{O}$ (Glew, 2002; Huo et al., 2003) and with field surveys of gas hydrates recovered offshore Japan and offshore India, which measure $0.139 < \chi < 0.141$, or $\text{CH}_4 \cdot (6.1\text{--}6.2)\text{H}_2\text{O}$ (Kida et al., 2015, 2018).

Our theoretical analysis suggests that hydrate nonstoichiometry could be used to infer the hydrate formation environment via careful compositional studies of recovered hydrates. The compositional distinction between hydrate formed from free gas versus dissolved phase is maximized at the moment of hydrate formation. In quiescent environments where hydrate has sufficient time to equilibrate with water (Ebinuma et al., 2005; Hyodo et al., 2017; Kneafsey et al., 2011), such compositional details have been shown to diminish over time through diffusion in order to establish hydrate-water equilibrium (Circone et al., 2005). However, in environments where hydrate formation is being fed by active gaseous methane flow, such as that of hydrated-crust gas bubble plumes (Wang et al., 2016), seeps, and seafloor outcrops (Bünz et al., 2012; Haeckel et al., 2004; Linke et al., 1994; Macelloni et al., 2012; Plaza-Faverola et al., 2015, 2017; Riedel et al., 2018; Suess et al., 1999; Smith et al., 2014), and gas chimneys (Andreassen et al., 2017; Haeckel et al., 2004; Liu & Flemings, 2006), the compositional gradient in the hydrate is likely sustained by the nonequilibrium nature of interfacial hydrate formation. While in situ measurements of hydrate compositions in these environments are less accessible, our results suggest that xenon is a good laboratory analog to methane in order to understand how hydrate formers transport through these geologic multiphase settings. Measuring and understanding compositional dynamics of hydrates that formed under gas-excess conditions will help us interpret methane venting rhythms around the world's oceans, infer gas flux dynamics, and assess the role of persistent seafloor methane discharge in the global carbon cycle.

The analogy between methane and xenon hydrate systems also raises the interesting possibility of addressing the following question: To provide insight on a particular methane hydrate occurrence existing at some pressure, temperature, and composition (p, T, χ) condition in the field, what conditions should one use to create an analogous xenon-hydrate experiment in the laboratory? We envision that one can address this question by first mapping the hydrate-forming conditions from one guest molecule (methane) to another (xenon) in the (p, T, χ) diagram, and then establishing an approximate time scaling that captures the difference in kinetic rate of hydrate formation between the two systems. While developing of such a thermodynamic equilibrium map and kinetics scaling is beyond the scope of this study, it is an exciting prospect for future work, which would facilitate the design of analog laboratory experiments.

Acknowledgments

This work was funded in part by the U.S. Department of Energy, DOE [awards DE-FE0013999 and DE-SC0018357 (to R. J.) and DOE Interagency Agreement DE-FE0023495 (to W. F. W.)]. X. F. acknowledges support by the Miller Research Fellowship at the University of California Berkeley. W. F. W. acknowledges support from the U.S. Geological Survey's Gas Hydrate Project and the Survey's Coastal, Marine Hazards and Resources Program. L. C. F. acknowledges funding from the Spanish Ministry of Economy and Competitiveness (grants RYC-2012-11704 and CTM2014-54312-P). L. C. F. and R. J. acknowledge funding from the MIT International Science and Technology Initiatives, through a Seed Fund grant. The simulation data are available on the UC Berkeley Dash repository at <https://doi.org/10.6078/D1G67B>.

References

- Andreassen, K., Hubbard, A., Winsborrow, M. C. M., Patton, H., Vadakkepuliambatta, S., Plaza-Faverola, A., et al. (2017). Massive blow-out craters formed by hydrate-controlled methane expulsion from the Arctic seafloor. *Science*, 356, 948–953.
- Ballard, A. L., & Sloan, E. D. (2002). The next generation of hydrate prediction: I. Hydrate standard states and incorporation of spectroscopy. *Fluid Phase Equilibria*, 194–197, 371–383.
- Ballard, A. L., & Sloan, E. D. (2004a). The next generation of hydrate prediction: Part III. Gibbs energy minimization formalism. *Fluid Phase Equilibria*, 218(1), 15–31.
- Ballard, A. L., & Sloan, E. D. (2004b). The next generation of hydrate prediction IV: A comparison of available hydrate prediction programs. *Fluid Phase Equilibria*, 216(2), 257–270.
- Buffett, B. A., & Zatsepina, O. Y. (2000). Formation of gas hydrate from dissolved gas in natural porous media. *Marine Geology*, 164(1–2), 69–77.

- Bünz, S., Polyanov, S., Vadakkepuliambatta, S., Consolaro, C., & Mienert, J. (2012). Active gas venting through hydrate-bearing sediments on the Vestnesa Ridge, offshore W-Svalbard. *Marine Geology*, 332-334, 189–197.
- Cahn, J. W., & Hilliard, J. E. (1958). Free energy of a nonuniform system. I. Interfacial free energy. *The Journal of Chemical Physics*, 28(2), 258.
- Chaouachi, M., Falenty, A., Sell, K., Enzmann, F., Kersten, M., Harberthür, D., & Kuhs, W. F. (2015). Microstructural evolution of gas hydrates in sedimentary matrices observed with synchrotron X-ray computed tomographic microscopy. *Geochemistry, Geophysics, Geosystems*, 16, 1711–1722. <https://doi.org/10.1002/2015GC005811>
- Chaouachi, M., Neher, S. H., Falenty, A., & Kuhs, W. F. (2017). Time resolved coarsening of clathrate crystals: The case of gas hydrates. *Crystal Growth & Design*, 17(5), 2458–2472.
- Chen, X., & Espinoza, D. N. (2018). Ostwald ripening changes the pore habit and spatial variability of clathrate hydrate. *Fuel*, 214(November 2017), 614–622.
- Chen, L. T., Li, N., Sun, C. Y., Chen, G. J., Koh, C. A., & Sun, B. J. (2017). Hydrate formation in sediments from free gas using a one-dimensional visual simulator. *Fuel*, 197, 298–309.
- Chen, X., Verma, R., Espinoza, N., & Prodanović, M. (2017). Pore-scale determination of gas relative permeability in hydrate-bearing sediments using X-Ray computed micro-tomography and lattice Boltzmann method. *Water Resources Research*, 54, 600–608. <https://doi.org/10.1002/2017WR021851>
- Circone, S., Kirby, S. H., & Stern, L. A. (2005). Direct measurement of methane hydrate composition along the hydrate equilibrium boundary. *Journal of Physical Chemistry B*, 109(19), 9468–9475.
- Cogswell, D. A., & Carter, W. C. (2011). Thermodynamic phase-field model for microstructure with multiple components and phases: The possibility of metastable phases. *Physical Review E*, 83(6), 1–13.
- Collett, T. S., Johnson, A. H., Knapp, C. C., & Boswell, R. (2009). Natural gas hydrates : A review. Natural gas hydrates—energy resource potential and associated geologic hazards: AAPG Memoir 89.
- Ebinuma, T., Kamata, Y., Minagawa, H., Ohmura, R., Nagao, J., & Narita, H. (2005). Mechanical properties of sandy sediment containing methane hydrate. In *Proceedings of the 5th international conference on gas hydrates* (pp. 958–961). Trondheim, Norway.
- Freer, E. M., Selim, M. S., & Sloan, E. D. (2001). Methane hydrate film growth kinetics. *Fluid Phase Equilibria*, 185, 65–75.
- Fu, X., Cueto-felgueroso, L., & Juanes, R. (2018). Nonequilibrium thermodynamics of hydrate growth on a gas-liquid interface. *Physical Review Letters*, 120(14), 144501.
- Glew, D. N. (2002). Aqueous nonelectrolyte solutions. Part XVIII. Equilibrium pressures of two methane hydrates with water. Formulae and dissociation thermo-dynamic functions for the structures I and II methane hydrates. *Canadian Journal of Chemistry*, 80(4), 418–439.
- Haeckel, M., Suess, E., Wallmann, K., & Rickert, D. (2004). Rising methane gas bubbles form massive hydrate layers at the seafloor. *Geochimica et Cosmochimica Acta*, 68(21), 4335–4345.
- Huo, Z., Hester, K., Sloan, E. D., & Miller, K. T. (2003). Methane hydrate nonstoichiometry and phase diagram. *AIChE Journal*, 49(5), 1300–1306.
- Hyo, M., Wu, Y., Nakashima, K., Kajiyama, S., & Nakata, Y. (2017). Influence of fines content on the mechanical behavior of methane hydrate-bearing sediments. *Journal of Geophysical Research: Solid Earth*, 122, 7511–7524. <https://doi.org/10.1002/2017JB014154>
- Jager, M. D., Ballard, A. L., & Sloan, E. D. (2003). The next generation of hydrate prediction: II. Dedicated aqueous phase fugacity model for hydrate prediction. *Fluid Phase Equilibria*, 211(1), 85–107.
- Jin, Y., Nagao, J., Hayashi, J., Shimada, W., Ebinuma, T., & Narita, H. (2008). Observation of Xe hydrate growth at gas-ice interface by microfocus X-ray computed tomography. *Journal of Physical Chemistry C*, 112(44), 17,253–17,256.
- Jung, J.-W., & Santamarina, J. C. (2012). Hydrate formation and growth in pores. *Journal of Crystal Growth*, 345(1), 61–68.
- Kennan, R. P., & Pollack, G. L. (1990). Pressure dependence of the solubility of nitrogen, argon, krypton, and xenon in water. *The Journal of Chemical Physics*, 93(4), 2724–2735.
- Kida, M., Jin, Y., Watanabe, M., Konno, Y., Yoneda, J., Egawa, K., et al. (2015). Chemical and crystallographic characterizations of natural gas hydrates recovered from a production test site in the eastern Nankai Trough. *Marine and Petroleum Geology*, 66, 396–403.
- Kida, M., Jin, Y., Yoneda, J., Oshima, M., Kato, A., Konno, Y., et al. (2018). Crystallographic and geochemical properties of natural gas hydrates accumulated in the National Gas Hydrate Program Expedition 02 drilling sites in the Krishna-Godavari Basin off India. *Marine and Petroleum Geology*. <https://doi.org/10.1016/j.marpetgeo.2018.10.012>
- Kneafsey, T. J., Seol, Y., Gupta, A., & Tomutsa, L. (2011). Permeability of laboratory-formed methane-hydrate-bearing sand: measurements and observations using X-ray computed tomography. *SPE Journal*, 16(1), 78–94.
- Lee, J. Y., Yun, T. S., Santamarina, J. C., & Ruppel, C. (2007). Observations related to tetrahydrofuran and methane hydrates for laboratory studies of hydrate-bearing sediments. *Geochemistry, Geophysics, Geosystems*, 8, Q06003. <https://doi.org/10.1029/2006GC001531>
- Lei, L., & Santamarina, J. C. (2018). Laboratory strategies for hydrate formation in fine-grained sediments. *Journal of Geophysical Research: Solid Earth*, 123, 2583–2596. <https://doi.org/10.1002/2017JB014624>
- Li, S.-L., Sun, C.-Y., Liu, B., Li, Z.-Y., Chen, G.-J., & Sum, A. K. (2014). New observations and insights into the morphology and growth kinetics of hydrate films. *Scientific Reports*, 4, 4129.
- Linke, P., Suess, E., Torres, M., Martens, V., Rugh, W. D., Ziebis, W., & Kulm, L. D. (1994). In situ measurement of fluid flow from cold seeps at active continental margins. *Deep-Sea Research Part I*, 41(4), 721–739.
- Liu, X., & Flemings, P. B. (2006). Passing gas through the hydrate stability zone at southern Hydrate Ridge, offshore Oregon. *Earth and Planetary Science Letters*, 241(1-2), 211–226.
- Lu, W., Chou, I. M., & Burruss, R. C. (2008). Determination of methane concentrations in water in equilibrium with sI methane hydrate in the absence of a vapor phase by in situ Raman spectroscopy. *Geochimica et Cosmochimica Acta*, 72(2), 412–422.
- Macelloni, L., Simonetti, A., Knapp, J. H., Knapp, C. C., Lutken, C. B., & Lapham, L. L. (2012). Multiple resolution seismic imaging of a shallow hydrocarbon plumbing system, Woolsey Mound, Northern Gulf of Mexico. *Marine and Petroleum Geology*, 38(1), 128–142.
- Meyer, D. W., Flemings, P. B., & DiCarlo, D. (2018). Effect of gas flow rate on hydrate formation within the hydrate stability zone. *Journal of Geophysical Research: Solid Earth*, 123, 6263–6276. <https://doi.org/10.1029/2018JB015878>
- Meyer, D. W., Flemings, P. B., DiCarlo, D., You, K., Phillips, S. C., & Kneafsey, T. J. (2018). Experimental investigation of gas flow and hydrate formation within the hydrate stability zone. *Journal of Geophysical Research: Solid Earth*, 123, 5350–5371. <https://doi.org/10.1029/2018JB015748>
- Moelans, N. (2011). A quantitative and thermodynamically consistent phase-field interpolation function for multi-phase systems. *Acta Materialia*, 59(3), 1077–1086.
- Nestler, B., Wheeler, A. A., Ratke, L., & Stöcker, C. (2000). Phase-field model for solidification of a monotectic alloy with convection. *Physica D*, 141, 133–154.
- Ohgaki, K., Sugahara, T., Suzuki, M., & Jindai, H. (2000). Phase behavior of xenon hydrate system. *Fluid Phase Equilibria*, 175(1-2), 1–6.

- Peters, B., Zimmermann, N. E. R., Beckham, G. T., Tester, J. W., & Trout, B. L. (2008). Path sampling calculation of methane diffusivity in natural gas hydrates from a water-vacancy assisted mechanism. *Journal of the American Chemical Society*, *130*(51), 17,342–17,350.
- Plaza-Faverola, A., Bunz, S., Johnson, J. E., Chand, S., Knies, J., Mienert, J., & Franek, P. (2015). Role of tectonic stress in seepage evolution along the gas hydrate-charged Vestnesa Ridge, Fram Strait. *Geophysical Research Letters*, *42*, 733–742. <https://doi.org/10.1002/2014GL062474>
- Plaza-Faverola, A., Vadakkepuliambatta, S., Hong, W. L., Mienert, J., Bünz, S., Chand, S., & Greinert, J. (2017). Bottom-simulating reflector dynamics at Arctic thermogenic gas provinces: an example from Vestnesa Ridge, offshore west Svalbard. *Journal of Geophysical Research: Solid Earth*, *122*, 4089–4105. <https://doi.org/10.1002/2016JB013761>
- Priegnitz, M., Thaler, J., Spangenberg, E., Schicks, J. M., Schrötter, J., & Abendroth, S. (2015). Characterizing electrical properties and permeability changes of hydrate bearing sediments using ERT data. *Geophysical Journal International*, *202*(3), 1599–1612.
- Riedel, M., Scherwath, M., Römer, M., Veloso, M., Heesemann, M., & Spence, G. D. (2018). Distributed natural gas venting offshore along the Cascadia margin. *Nature Communications*, *9*(1), 3264.
- Ruppel, C., & Kessler, J. D. (2017). The interaction of climate change and methane hydrates. *Reviews of Geophysics*, *55*, 126–168. <https://doi.org/10.1002/2016RG000534>
- Sahoo, S. K., Madhusudhan, B. N., Marín-Moreno, H., North, L. J., Ahmed, S., Falcon-Suarez, I. H., et al. (2018). Laboratory insights into the effect of sediment-hosted methane hydrate morphology on elastic wave velocity from time-lapse 4D synchrotron X-ray computed tomography. *Geochemistry, Geophysics, Geosystems*, *19*, 4502–4521. <https://doi.org/10.1029/2018GC007710>
- Sahoo, S. K., Marín-Moreno, H., North, L. J., Falcon-Suarez, I., Madhusudhan, B. N., Best, A. I., & Minshull, T. A. (2018). Presence and consequences of coexisting methane gas with hydrate under two phase water-hydrate stability conditions. *Journal of Geophysical Research: Solid Earth*, *123*, 3377–3390. <https://doi.org/10.1029/2018JB015598>
- Sanloup, C., Mao, H.-K., & Hemley, R. J. (2002). High-pressure transformations in xenon hydrates. *Proceedings of the National Academy of Sciences of the United States of America*, *99*(1), 25–28.
- Sloan, E. D., & Koh, C. A. (2008). *Clathrate Hydrates of Natural Gases* (3rd ed.). Boca Raton, FL: CRC Press.
- Sloan, E. D., Koh, C. A., & Sum, A. K. (2010). Gas hydrate stability and sampling: The future as related to the phase diagram. *Energies*, *3*(12), 1991–2000.
- Smith, A. J., Mienert, J., Bünz, S., & Greinert, J. (2014). Thermogenic methane injection via bubble transport into the upper Arctic Ocean from the hydrate-charged Vestnesa Ridge, Svalbard. *Geochemistry, Geophysics, Geosystems*, *15*, 1945–1959. <https://doi.org/10.1002/2013GC005179>
- Spangenberg, E., & Kulenkampff, J. (2006). Influence of methane hydrate content on electrical sediment properties. *Geophysical Research Letters*, *33*, L24315. <https://doi.org/10.1029/2006GL028188>
- Stern, L. A., Kirby, S. H., & Durham, W. B. (1996). Peculiarities of methane clathrate hydrate formation and solid-state deformation, including possible superheating of water ice. *Science*, *273*(September), 1843–1848.
- Suess, E., Torres, M. E., Bohrmann, G., Collier, R. W., Greinert, J., Linke, P., et al. (1999). Gas hydrate destabilization: Enhanced dewatering, benthic material turnover and large methane plumes at the Cascadia convergent margin. *Earth and Planetary Science Letters*, *170*(1–2), 1–15.
- Sum, A. K., Koh, C. A., & Sloan, E. D. (2012). Developing a comprehensive understanding and model of hydrate in multiphase flow: From laboratory measurements to field applications. *Energy Fuels*, *26*(7), 4046–4052.
- Tanaka, R., Sakemoto, R., & Ohmura, R. (2009). Crystal growth of clathrate hydrates formed at the interface of liquid water and gaseous methane, ethane, or propane: Variations in crystal morphology. *Crystal Growth & Design*, *9*(5), 2529–2536.
- Taylor, C. J., Miller, K. T., Koh, C. A., & Sloan, E. D. (2007). Macroscopic investigation of hydrate film growth at the hydrocarbon/water interface. *Chemical Engineering Science*, *62*(23), 6524–6533.
- Waite, W. F., & Spangenberg, E. (2013). Gas hydrate formation rates from dissolved-phase methane in porous laboratory specimens. *Geophysical Research Letters*, *40*, 4310–4315. <https://doi.org/10.1002/grl.50809>
- Waite, W. F., Weber, T., Fu, X., Juanes, R., & Ruppel, C. (2017). Laboratory observations of the evolution and rise rate of bubbles with and without hydrate shells. In *Proceedings of the 9th international conference on gas hydrates, Denver, USA*.
- Wang, B., Socolofsky, S., Breier, J., & Seewald, J. (2016). Observations of bubbles in natural seep flares at MC 118 and GC 600 using in situ quantitative imaging. *Journal of Geophysical Research: Oceans*, *121*, 2203–2230. <https://doi.org/10.1002/2015JC011452>
- Warzinski, R. P., Lynn, R., Haljasmaa, I., Leifer, I., Shaffer, F., Anderson, B. J., & Levine, J. S. (2014). Dynamic morphology of gas hydrate on a methane bubble in water: Observations and new insights for hydrate film models. *Geophysical Research Letters*, *41*, 6841–6847. <https://doi.org/10.1002/2014GL061665>
- Wilson, G. (1964). A new expression for the excess free energy of mixing. *Journal of the American Chemical Society*, *86*(2), 127–130.
- Witherspoon, P. A., & Saraf, D. N. (1965). Diffusion of methane, ethane, propane, and n-butane. *The Journal of Physical Chemistry*, *69*(11), 3752–3755.
- Yang, L., Falenty, A., Chaouachi, M., Harberthür, D., & Kuhs, W. F. (2016). Synchrotron X-ray computed microtomography study on gas hydrate decomposition in a sedimentary matrix. *Geochemistry, Geophysics, Geosystems*, *17*, 3717–3732. <https://doi.org/10.1002/2016GC006521>
- Zatsepina, O. Y., & Buffett, B. A. (1997). Phase equilibrium of gas hydrate: Implications for the formation of hydrate in the deep sea floor. *Geophysical Research Letters*, *24*(13), 1567–1570.
- Zatsepina, O. Y., & Buffett, B. A. (1998). Thermodynamic conditions for the stability of gas hydrate in the seafloor. *Journal of Geophysical Research*, *103*, 24,127–24,139.